# Air-sea interactions and water mass transformation during a katabatic storm in the Irminger Sea

**O. Gutjahr[1,2], J. H. Jungclaus[2], N. Brüggemann[1,2], H. Haak[2], J. Marotzke[2,3]**

[1]Institut für Meereskunde, Universität Hamburg, Hamburg, Germany.
[2]Max Planck Institute for Meteorology, The Ocean in the Earth System, Hamburg, Germany.
[3]Center for Earth System Research and Sustainability (CEN), Universität Hamburg, Germany.

**Key Points:**

- For the first time, the direct effect of a katabatic storm on the ocean has been simulated in a global climate model
- The katabatic storm triggers a polar low and develops in positive feedback with it
- Katabatic storms induce water mass transformation over the shelf and boundary current that contributes to the North Atlantic Deep Water

Corresponding author: O. Gutjahr, oliver.gutjahr@mpimet.mpg.de

**Abstract**

We use a global 5-km resolution model to analyse the air-sea interactions during a katabatic storm in the Irminger Sea originating from the Ammassalik valleys. Katabatic storms have not yet been resolved in global climate models, raising the question of whether and how they modify water masses in the Irminger Sea. Our results show that dense water forms along the boundary current and on the shelf during the katabatic storm due to the heat loss caused by the high wind speeds and the strong temperature contrast. The dense water contributes to the North Atlantic Deep Water and thus to the Atlantic Meridional Overturning Circulation (AMOC). The katabatic storm triggers a polar low, which in turn amplifies the near-surface wind speed in a positive feedback, in addition to acceleration from a breaking mountain wave. Resolving katabatic storms in global models is therefore important for the formation of dense water in the Irminger Sea, which is relevant to the AMOC, and for the large-scale atmospheric circulation by triggering polar lows.

## Plain Language Summary

Katabatic storms originating from the Ammassalik area in southeast Greenland have so far not been resolved in global climate models because their spatial extent is smaller than typical grid resolutions. We analyse a case study of an katabatic storm from a novel storm-resolving (5 km) simulation with the globally coupled ICON-ESM and demonstrate that this katabatic storm causes substantial heat loss in the Irminger Sea's boundary current, leading to dense water formation and sinking on the southeast Greenland shelf. These results suggest that resolving such katabatic storms in global models could affect the location and intensity of the sinking of the global conveyor belt in the subpolar North Atlantic.

## 1 Introduction

Recent observations made with the Overturning in the Subpolar North Atlantic Program (OSNAP) array allowed for the first time to directly relate deep water mass formation in the subpolar North Atlantic and overturning variability. These data indicate that water mass transformation east of Greenland is largely responsible for the overturning of the Atlantic Meridional Overturning Circulation (AMOC) and its variability (Lozier et al., 2019). However, the exact role of the Irminger and Labrador Sea in AMOC variability is still controversial. In particular, it is discussed whether deep water formation in the Labrador Sea contributes only marginally to AMOC variability (Desbruyères et al., 2019; Menary et al., 2020), whether there has been a shift in deep water formation from the Labrador to the Irminger Sea over the past decade (Rühs et al., 2021) or whether deep water formation in the Labrador Sea dominates multidecadal AMOC variability, while that in the Irminger Sea influences high-frequency variability (Yeager et al., 2021).

In the Irminger Sea, strong surface heat and momentum fluxes were found to be most important for generating density anomalies in the boundary currents, such as the East Greenland-Irminger Current (EGIC) or over the Reykjanes Ridge (LeBras et al., 2020; Petit et al., 2020). Based on OSNAP, an upper Irminger Sea Intermediate Water (uISIW; $\sigma_\theta = 27.65$ to $27.73\,\mathrm{kg\,m^{-3}}$) has been identified forming at the edge of the EGIC (LeBras et al., 2020). This intermediate water contributes to deep water formation alongside the denser water masses formed by deep convection in the basin interior (Bacon et al., 2003; Pickart et al., 2003; de Jong et al., 2012, 2018) and overflows from the Nordic Seas (Chafik & Rossby, 2019). The dense water anomalies from the boundary current are transported southward into the Labrador Sea where they correlate strongly with AMOC variability (Desbruyères et al., 2019; Petit et al., 2020; Menary et al., 2020).

However, the surface fluxes producing these density anomalies are likely underestimated in current global climate models, such as those involved in CMIP6 (Eyring et al., 2016) or in CMIP6 HighResMIP (Haarsma et al., 2016), because the wind systems that cause these strong fluxes are mesoscale and therefore not or insufficiently resolved. In particular, katabatic winds and storms originating from the Greenland Ice Sheet cause a strong loss of heat and buoyancy of the shelf water and EGIC due to the high wind speeds and the cold and dry air they carry over the relatively warm ocean. They contribute to about one fifth of the total winter heat loss (Oltmanns et al., 2014). Resolving katabatic storms could therefore affect the deep water formation in the Irminger Sea and hence its role for AMOC variability.

Katabatic winds are density-driven currents originating from large ice sheets, such as in Greenland, due to radiative cooling of the surface boundary layer. They dominate the near-surface wind field and their velocity is highest near the ice sheet margins. The strongest downslope katabatic winds occur frequently in the Ammassalik area on the southeast coast of Greenland, where the katabatic flow converges in the narrow fjords and accelerates because of the steep topography (Heinemann & Klein, 2002). This gravitational acceleration becomes stronger the colder and thus denser the air is. When a synoptic cyclone is located over the Irminger Sea, the overlying geostrophic flow can strengthen the pure katabatic flow to gale force, sometimes even hurricane force, which then causes severe destruction (Rasmussen, 1989; Oltmanns et al., 2014). Often these two mechanisms work together to form a katabatic storm. However, a third mechanism is the breaking of mountain or lee waves over the steep slopes of southeast Greenland (Oltmanns et al., 2015), which transfer momentum into the boundary layer and further accelerate the katabatic flow. These hazardous katabatic storms or "piteraqs" (Greenlandic) are a regular phenomena and the most severe on record was hitting the community of Tasiilaq (Ammassalik) in February 1970 with a peak velocity of nearly $90\,\mathrm{m\,s^{-1}}$.

Over the Irminger Sea, katabatic winds from Ammassalik can trigger mesocyclones (Klein & Heinemann, 2002), also called polar lows (Kolstad, 2011; Moreno-Ibáñez et al., 2021). Polar lows frequently form over the Irminger Sea (Bracegirdle & Gray, 2008; Zahn & von Storch, 2008; Kolstad, 2011; Stoll et al., 2018), which is related to cyclogenisis in the lee of Greenland's high orography (Blechschmidt et al., 2009; Kristjánsson et al., 2011) and with marine cold air outbreaks (MCAO, Kolstad et al., 2009), including katabatic winds (Klein & Heinemann, 2002). In particular, two mechanisms are at work (Klein & Heinemann, 2002). First, the convergence of the katabatic flow in the valleys lead to vortex stretching that enhances cyclonic vorticity that is transported eastward by the horizontal flow. Second, advection of cold air from the Greenland ice sheet over the relatively warm Irminger Sea leads to high sensible and latent heat fluxes, whose divergences reduce the atmospheric stratification. If clouds form over the Irminger Sea because of the large latent heat fluxes, atmospheric stratification is further reduced due to release of latent heat. Katabatic winds from Ammassalik therefore increase low-level baroclinicity that favours the formation of polar lows.

On average, about 5 to 11 polar lows form in the Irminger Sea per winter, depending on the detecting method and data set analysed (Zahn & von Storch, 2008; Kolstad, 2011), while katabatic storms in the Ammassalik area occur about seven times per year, reaching about $20\,\mathrm{m\,s^{-1}}$ (Oltmanns et al., 2014). If sea ice is present, katabatic winds from the Ammassalik valleys can open coastal polynyas (Heinemann, 2003). The brine released during the formation of new sea ice then contributes to even denser shelf waters. Katabatic winds may also be important for fluxing fresh shelf water of Arctic origin into the interior basin of the Irminger Sea, thereby affecting the stratification. How exactly freshwater is transported off-shelf is still unclear, but wind is thought to be the main driver (Duyck & de Jong, 2021).

Resolving katabatic storms and small-scale orographic features in GCMs is therefore crucial for the cooling and densification of the EGIC, but also for the feedback of

small-scale processes to the synoptic scale in terms of polar low formation and exchange of momentum and energy. Because of the teleconnectivity that the Irminger Sea exerts on the AMOC and the large-scale atmospheric circulation, a global coupled model is needed to capture these interactions. However, the atmospheric resolution of CMIP6 models is on the order of 50 to 100 km, with some exceptions of 25 km for individual HighResMIP models. Katabatic winds and other mesoscale wind systems around Greenland, such as tip jets, require model resolutions of less than 10 to 15 km to be adequately represented (DuVivier & Cassano, 2013; Oltmanns et al., 2015; Gutjahr & Heinemann, 2018). A resolution of 5 km is even better to capture the channelling effects in the narrow fjords and the momentum transfer by breaking mountain waves over the steep coastal slopes (Oltmanns et al., 2015). Katabatic winds further require a high vertical resolution in the surface boundary layer where also low-level jets form (Heinemann, 2003). In addition, a non-hydrostatic dynamical core is needed to simulate the strong vertical velocities during a katabatic storm, especially where mountain waves breaks causing a katabatic jump and generating gravity waves.

Since a high resolution is required, katabatic storms have so far only been studied with regional atmosphere models (e.g. Oltmanns et al., 2014, 2015). Even though high model resolution can be achieved in regional models, they have two severe limitations. First, they were used as stand-alone, i.e. they were not coupled to an ocean model, thereby neglecting air-sea interactions with the ocean, including changes to the circulation and the water mass characteristics. Second, because of their limited domain they do not allow for feeding back the effects of the small scales to the large scales, thereby neglecting teleconnections. Although the interactions across scales is sometimes realized in regional models by so-called two-way nesting, the problem remains that the rest of the globe is not affected by the resolved small scales within the domain. Similar arguments apply to studies with ocean stand-alone simulations, which must be driven by atmospheric data that cannot respond to feedbacks with the ocean and are often too coarse to represent the mesoscale winds around Greenland (e.g. Paquin et al. (2016)).

Since the resolution of global climate models has so far been too coarse to resolve katabatic storms (Mc Innes et al., 2011), their influence on the EGIC was likely underestimated. Although there were attempts to account for their effects on the ocean circulation (Condron et al., 2008), such parameterizations were never widely used in global models. Here we analyze for the first time a katabatic storm or piteraq that triggers a polar low, interacts with it and causes water mass transformation in the Sermilik Trough (ST) and EGIC. We exploit a frontier simulation with the globally coupled, storm- and eddy-resolving (5 km) ICON-ESM, which is almost two years long. An overview of the simulation will be presented elsewhere.

The analyzed katabatic storm is the most intense in simulation, which is why we chose it for our case study. Even though the simulation is too short to link density anomalies in the boundary current to the AMOC, the model is potentially able to simulate this linkage.

The remainder of the manuscript is organized as follows: in section 2 we describe the model configuration, section 3 outlines the development of the katabatic storm, in section 4 and 5 the analyses of the air-sea interactions and induced response of the ocean are presented. We conclude in section 6.

## 2 Model configuration

We analyze the development of a katabatic storm in the Irminger Sea and its induced air-sea fluxes and water mass transformation in a frontier simulation made with ICON-ESM (ICOsahedral Non-hydrostatic - Earth System Model; Zängl et al. (2015); Korn (2017); Giorgetta et al. (2018); Jungclaus et al. (2021)), which is participating in

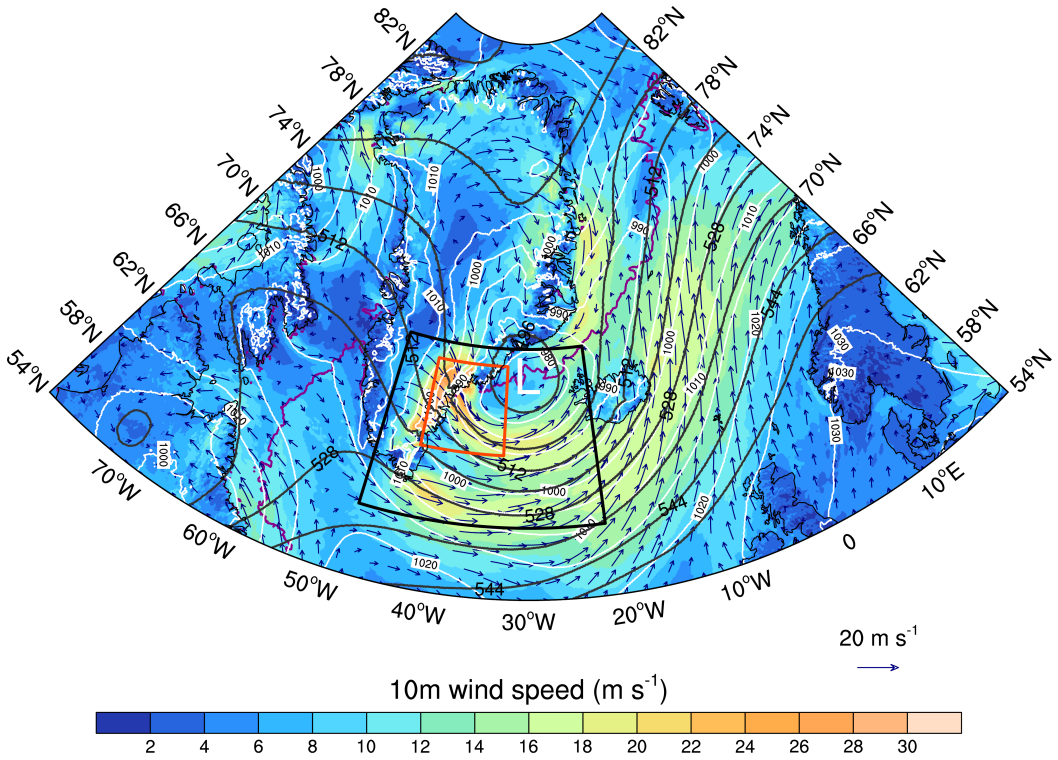


**Figure 1.** Synoptic situation on simulation day for 29 February 2020 in ICON-ESM. Shown is the daily mean of 10 m wind speed (colour shaded) and the wind vectors. Overlain is the daily mean sea-level pressure in hPa (white contours), the geopotential height at 500 hPa in gpdm (dark grey contours), and the 15 % sea ice concentration (magenta contour). The reference scale of the wind vectors is given at the bottom right. The "L" symbol marks the centre of the polar low that is moving towards Denmark Strait. The black box marks the area of the Irminger Sea and the orange box the Ammassalik area.

the second phase of the DYnamics of the Atmospheric general circulation On Non-hydrostatic Domains (DYAMOND) Winter initiative (Stevens et al., 2019, and `https://www.esiwace.eu/services/dyamond/winter`). The model is globally coupled and was run at a horizontal resolution of 5 km, both in the non-hydrostatic atmospheric component (ICON-A) and in the hydrostatic ocean/sea ice component (ICON-O). The grid resolution is thereby defined as the square root of the cell area of the spherical triangles (Zängl et al., 2015). Both components use a high vertical resolution. ICON-A is run with 90 terrain-following, hybrid sigma levels, with the top layer at 75 km height, which corresponds to the operational weather forecast configuration at Deutscher Wetterdienst (DWD). Thirteen levels are distributed within the lower 2000 m over the Irminger Sea and 20 levels over land in the Ammassalik area. ICON-O uses 128 z-levels without a partial bottom cell parameterization. Ninety-six levels are distributed within the upper 500 m.

A main purpose of the DYAMOND (Winter) initiative is to run atmosphere models at a convection and storm resolving resolution ($\leq 5$ km) and the ocean models at a similar resolution. The vertical resolution must be at least 75 levels in both spheres in order to study the mesoscale ocean-atmosphere coupling. Although the model resolution approaches the km scale, the smallest scale that is fully resolved in the model - the effective resolution - is much larger than the grid spacing or nominal model resolution. The effective resolution is usually determined by comparing modeled and observed ki-

netic energy spectra (Skamarock, 2004). For ICON-A, the effective resolution is about 7 times the mesh size (Zängl et al., 2015; Neumann et al., 2019), which corresponds to 35 km for our configuration. Below this scale, kinetic energy is dissipated due to physical parameterizations, orographic smoothing, numerical diffusion and aliasing effects (Neumann et al., 2019; Klaver et al., 2020). Therefore, small-scale atmospheric processes, such as convection or orographic drag, are still partially unresolved in this model configuration. However, studies with regional models have shown that a nominal model resolution of less than 10 to 15 km is sufficient to resolve the main features of mesoscale wind systems around Greenland (DuVivier & Cassano, 2013; Gutjahr & Heinemann, 2018) and that 5 km is sufficient for the representation of katabatic storms (Oltmanns et al., 2014, 2015).

For ICON-O there has been no quantification of the effective resolution yet. With reference to the first baroclinic Rossby deformation radius calculated by LaCasce and Groeskamp (2020), which also takes bathymetry into account, we find a required resolution to resolve eddies of about $1/25\,^\circ$ to $1/12\,^\circ$ in the Irminger Sea (about 5 km to 2 km at $60\,^\circ$N) and $1/50\,^\circ$ (about 1 km) over the shelf.

ICON-A was run with the ECHAM6.3 physics (Giorgetta et al., 2018) and not with the Numerical Weather Prediction (NWP) physics. The reason is that the ECHAM6.3 physics is largely energy conserving, which is a necessity for studying coupled processes and climate. However, to account for the storm resolving resolution, several adjustments were made to the physical parameterizations in ICON-A. First, the atmospheric deep convection scheme was switched off. Further, parameterizations of subgrid-scale orographic effects (blocking and gravity wave drag) and non-orographic gravity wave drag were switched off and cloud microphysics were calculated using a three-category ice scheme, referred to as the graupel scheme. On the other hand, atmospheric subgrid-scale turbulence was parameterized with the 3D-Smagorinsky scheme, which has been implemented into ICON-A for large eddy simulation applications (Dipankar et al., 2015). In ICON-O, the mesoscale eddy parameterization (Gent-McWilliams (GM) closure) was switched off and vertical mixing was parameterized with the turbulent kinetic energy (TKE) closure (Gaspar et al., 1990; Blanke & Delecluse, 1993).

Before coupling, both components were spun up separately. The atmosphere was initialized from the global (9 km) European Centre for Medium Range Weather Forecasts (ECMWF) Integrated Forecasting System (IFS) analysis corresponding to 20 January 2020. Spinning up the ocean is more expensive. Therefore, the following strategy was used for this first 5 km coupled simulation. The initial fields were taken from PHC3.0 (Steele et al., 2001) and interpolated to a coarser 10 km grid. The ocean was spun up on this coarser grid using a combination of different atmospheric forcing data. First, 25 cycles were run with OMIP forcing, a climatology based on the ERA-40 years 1958–2001 (Simmons & Gibson, 2000), followed by NCEP (Kalnay et al., 1996) from 1948 to 2000 and ERA5 (Hersbach et al., 2020) from 2000 to 2010. Then, the ocean state was interpolated from the 10 km to the 5 km grid and the 10 recent years (2011 to 2020) were forced with ERA5 (Hersbach et al., 2020) to ensure the development of background features, such as ocean mesoscale eddies or currents. We note that the spin-up was produced with an older model version and was not repeated with the version of the production run due to computational costs.

Once coupled, atmospheric fluxes were exchanged every 15 minutes. The model was run for 21 simulation months, starting from 20 January 2020 and ending on 30 September 2021. However, we focus on the first winter and in particular on the 29 February when the katabatic storm develops. Before analyzing the fields, all output data has been interpolated by the nearest neighbour method onto a regular grid of $0.05\,^\circ$.

Using a global simulation has the advantage of avoiding arbitrary domain boundaries, such as in regional models, which would inevitably introduce artefacts that could influence the process under investigation (Leduc & Laprise, 2009; Giorgi, 2019). In ad-

dition, due to the global high resolution, the synoptic fields and the background state of the ocean are expected to be more realistic than in comparable downscaling studies, where only the nested simulation is run at high resolution, while the parent simulation has a much coarser resolution. Furthermore, the small scales feed back to the large scales and thereby modify the synoptics.

## 3 Synoptic overview and katabatic storm development

We analyze a katabatic storm appearing on the simulation day of 29 February 2020 and that has no real-time counterpart. This storm is the strongest of roughly 15 similar events within the two simulation years, and its effect on the Irminger Sea is likely most pronounced, which is why it was chosen for our case study. During the simulation, no open ocean convection occurs in the Irminger Sea, and deeper mixed layers during winter are only simulated along the western flank of the Reykjanes Ridge (600 to 900 m) and along the EGIC (500 to 1300 m).

The storm develops when an upper-level trough crosses southeast Greenland. Within the westerly flow, a lee trough forms east of Cape Farewell, Greenland's southernmost tip. Within the lee trough, the katabatic flow from the Ammassalik area triggers a polar low. The synoptic pressure gradient on the backside of the polar low amplifies the katabatic winds in a positive feedback until the storm reaches near-surface wind speeds of more than $26\,\mathrm{m\,s^{-1}}$ (Fig. 1) and almost $50\,\mathrm{m\,s^{-1}}$ in the low-level jet at the boundary layer top.

On 28 February 2020 at 00 UTC, the centre of the upper-level trough is located over western Greenland (Fig.2a). The southeast coast of Greenland is below the cyclonic side of the diffluence zone of the jetstreak and hence an area favourable for upward motion and cyclogenesis. Upper-level divergence and differential vorticity advection cause upward motion diagnosed via the vorticity term in the $\omega$-equation. A LT forms east of Cape Farewell (Fig.2a) and further preconditions the southeast coast of Greenland for cyclogenesis (Kristjánsson et al., 2011). These lee throughs form frequently east of Cape Farewell in response to vortex stretching and potential vorticity (PV) conservation (Mc Innes et al., 2009) when the westerly flow descends adiabatically from the high orography of Greenland (Kristjánsson et al., 2011). A vertical transect along the Ikertivaq valley (Fig. 2b) shows only weak winds near the surface and a stable stratification with cloud cover below 2000 m.

Within the next 18 hours, the upper-level trough crosses southern Greenland and its centre deepens to 496 gpdm over the Irminger Sea (Fig. 2c), showing a strong cyclonic PV anomaly with more than 2 PVU at 500 hPa. At the surface, the pressure is falling in response to the upper-level divergence that induces low-level convergence (Hoskins et al., 1985; Bracegirdle & Gray, 2009). Katabatic flow is initiated by a superimposed pressure gradient over the Ammassalik valleys and cold air is drained from the Greenland ice sheet (Fig. 2d). Near the coast, the katabatic flow channels in the narrow valleys and accelerates. This converging flow constitutes a low-level baroclinic instability and enhances cyclonic vorticity due to vortex stretching, thereby increasing the PV anomaly (Klein & Heinemann, 2002). As a measure for baroclinicity we calculate the maximum Eady growth rate ($\sigma_{max}$ in $\mathrm{s^{-1}}$) (Eady, 1949; Lindzen & Farrell, 1980; Dierer & Schluenzen, 2005) that describes how well deep pressure systems can develop in a weather situation over a specific area, with positive values favouring cyclogenesis:

$$\sigma_{max} = 0.398 f \partial_z \boldsymbol{V}_h N^{-1}, \tag{1}$$

with $f$ the Coriolis parameter, $\partial_z \boldsymbol{V}_h$ the vertical wind shear, and $N = \sqrt{g/\theta \partial_z \theta}$ the buoyancy frequency that depends on the gravitational constant $g$ and the vertical

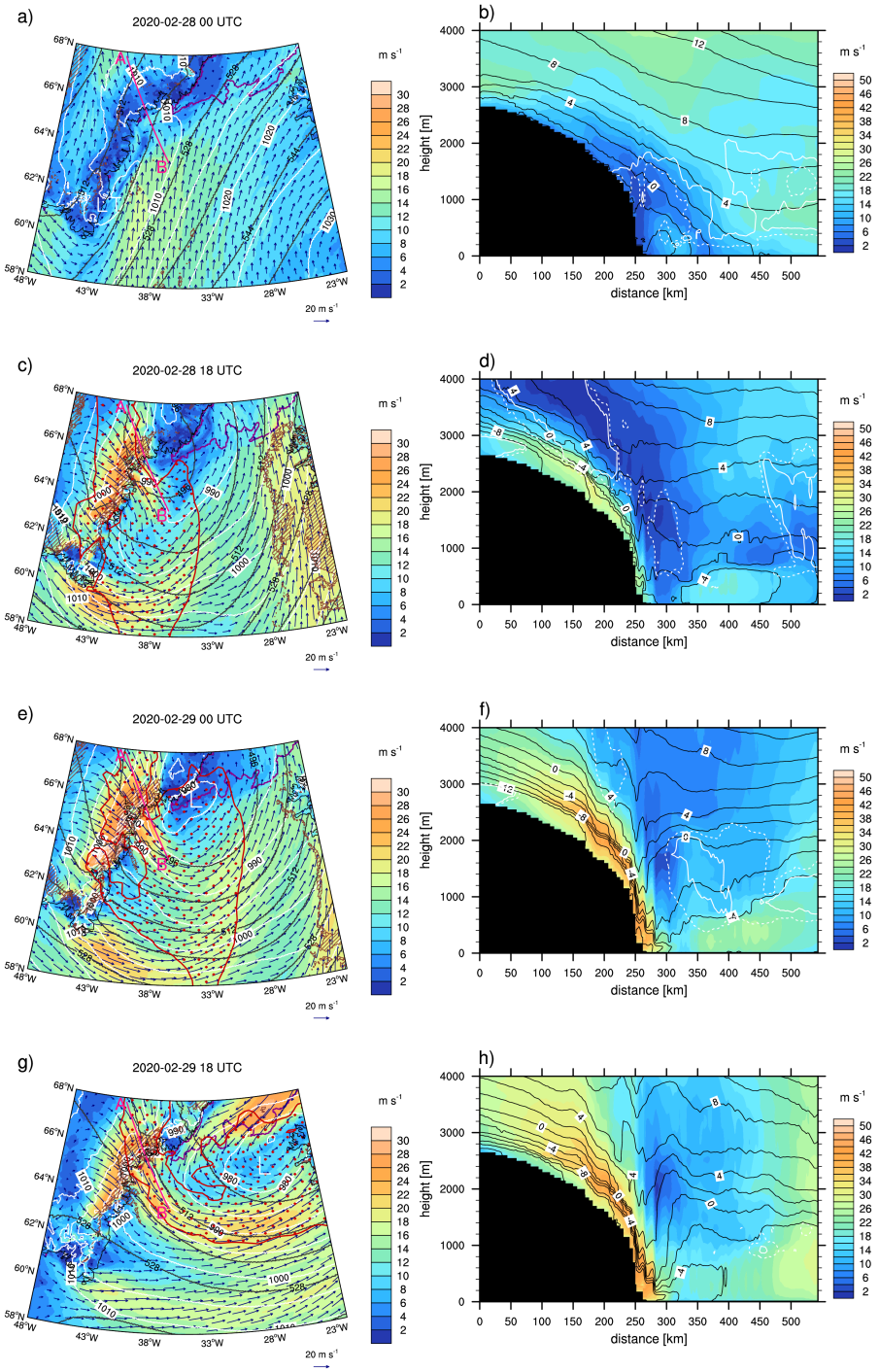


**Figure 2.** Development of the katabatic storm on 28 and 29 February 2020 in the Irminger Sea as simulated by ICON-ESM. The first column (a,c,e,g) shows the 10 m wind speed (6-hourly mean; colour shaded) and vectors, overlain by the mean-sea level pressure in hPa (white contours, every 5 hPa), the potential vorticity at 500 hPa ($\geq$2 PVU; 1 PVU $= 10^{-6}\,\mathrm{K\,m^2\,kg^{-1}\,s^{-1}}$; red contour and stippling), and the sea ice edge (15 % ice concentration, purple contour). "LT" in a) marks the lee trough east of Cape Farewell, and "L" in e) and g) the position of the polar low. Brown hatching marks areas where the Eady growth rate averaged over the lowest 2000 m is larger than $0.5 \cdot 10^{-4}\,\mathrm{s^{-1}}$. The second column (b,d,f,h) shows the transects of wind speed (shaded colour), potential temperature in $^{\circ}C$ (black contours) and cloud cover (25 % as dashed white contours, 50 % as solid white contours) through the Ikertivaq valley in the Ammassalik area (magenta line in first column).

gradient of the potential temperature $\theta$. The Ammassalik area is clearly a region of low-level baroclinicity as indicated by the positive Eady growth rate in Fig. 2c.

Within the next 6 hours, the katabatic flow from Ammassalik triggers a polar low with closed isobars on 29 February at 00 UTC and a core pressure of less than 980 hPa (Fig. 2e). Converging flow, cold-air advection decreasing with height, and the baroclinicity in the Ammassalik area trigger the formation of the polar low (Klein & Heinemann, 2002) near the sea ice edge, where polar lows frequently form and intensify (Dierer & Schluenzen, 2005; Bracegirdle & Gray, 2009). Furthermore, the coupling of the lower and upper-level PV anomalies reinforces the polar low, which in turn deepens the upper-level trough.

The Irminger Sea is known for polar low genesis and exhibits strong vertical temperature differences (Kristjánsson et al., 2011). Although there is no universal definition for a polar low (Kolstad, 2011), Blechschmidt et al. (2009) defined two criteria: 1) temperature difference between the surface and at 500 hPa ($SST-T_{500}$) of more than 48 K and 2) an upper-level cyclonic PV anomaly. From 6-hourly averages, we find both criteria roughly fulfilled with $SST-T_{500} = 45$ K (not shown) and a positive PV anomaly of more than 2 PVU at 500 hPa. Note that there are other thresholds used for the same criterion, such as 43 K (Xia et al., 2012) or 40 K (Landgren et al., 2019), or other definitions, such as the MCAO index ($SST-T_{700}$) (Kolstad et al., 2009). For our study, the exact threshold or definition is not decisive.

On the back side of the polar low, the superimposed pressure gradient intensifies, further accelerating the katabatic flow (Fig.2e) and draining increasingly cold air from the Greenland ice sheet. The cold air spreads as a tongue over the Irminger Sea, where it warms and causes atmospheric convection with cloud formation (Fig.2f). In addition, a mountain or lee wave breaks at the steep slope of the topography (roughly at 250 km distance) and transfers momentum downwards into the katabatic boundary layer (Oltmanns et al., 2015) that further accelerates the katabatic flow. Once the polar low reaches mature state (Fig.2g,h), the wind speed peaks with hurricane intensity of almost 50 m s$^{-1}$. The associated low-level jet is most intense near the top of the stable boundary layer. Although the highest near-surface wind speeds occur over the shelf, the storm affects the entire Irminger Sea, even reaching Iceland (Fig.2g).

These results suggest that four processes interact in the formation of the polar low and cause this katabatic storm: 1) favourable conditions for cyclogenesis due to an upper-level trough crossing South Greenland (upper-level divergence and positive vorticity advection or PV anomaly), 2) a lee trough east of Cape Farewell generating cyclonic vorticity due to vortex stretching, 3) triggering of a polar low by katabatic flow due to baroclinicity of the converging flow from the Ammassalik valleys and a positive feedback with the polar low that amplifies the katabatic flow, and 4) a breaking mountain wave that transfers momentum downward into the surface boundary layer and causes additional acceleration. Although we cannot generalize from this case study, it seems that all these processes are of importance in the polar low formation in the Irminger Sea and for generating katabatic storms of hurricane intensity.

## 4 Air-sea interactions and water mass transformation over the shelf and in the Irminger Sea

The katabatic storm with its high wind speeds is expected to substantially modify the water of the southeast Greenland shelf, but also the western boundary current, i.e. EGIC, and the upper ocean of the Irminger Basin, because the tongue of cold air and high wind speeds extends across the entire basin and even reaches the western flank of the Reykjanes Ridge (Fig. 2g).

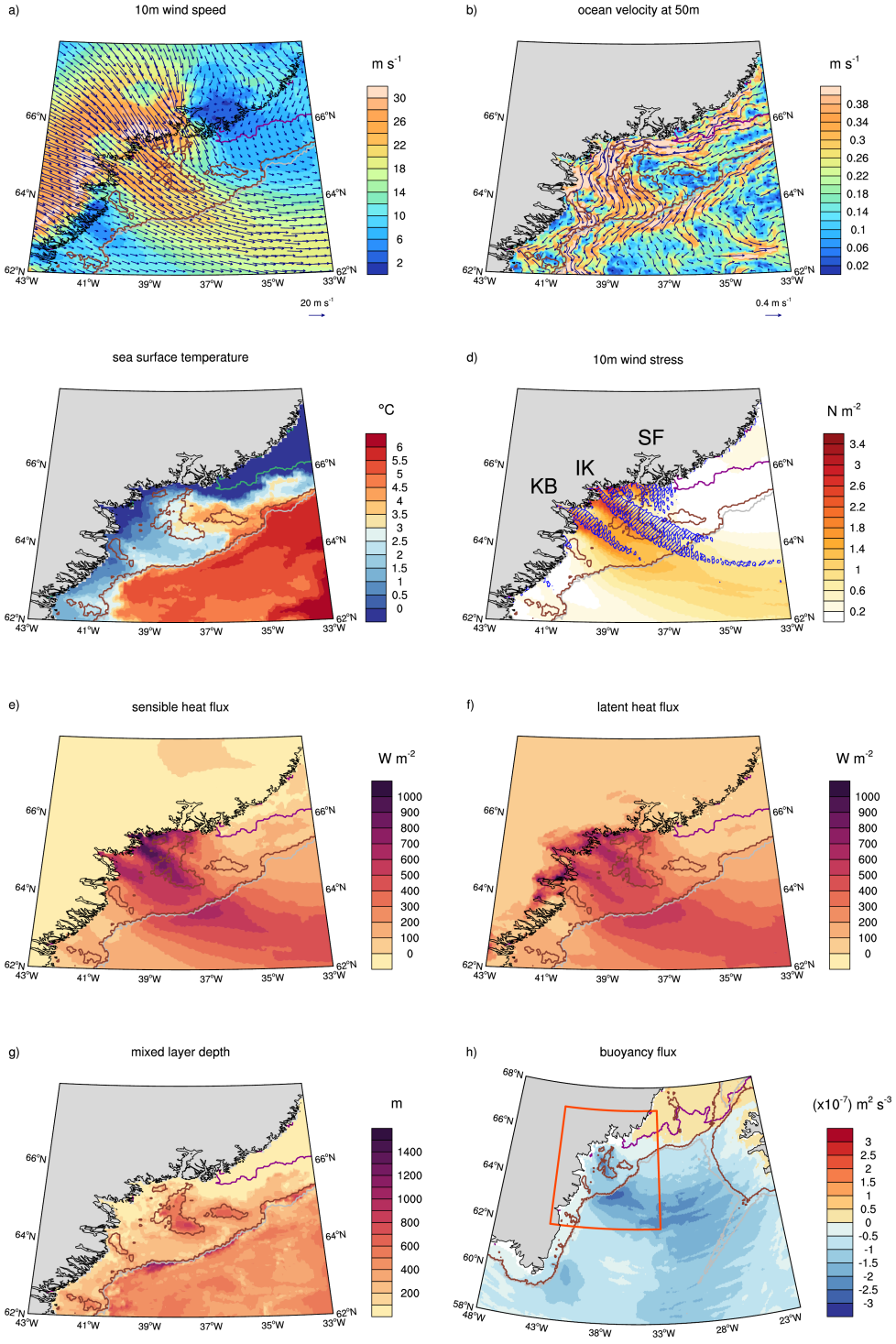


**Figure 3.** Air-sea interactions (daily means) in the Ammassalik area: a) 10 m wind speed (shaded colour) and vectors, b) ocean velocity at 50 m depth, c) sea surface temperature, d) 10 m wind stress and positive wind stress curl ($\leq \quad 0.15 \cdot 10^4\,\mathrm{N\,m^{-3}}$ as blue hatching), e) sensible heat flux, f) latent heat flux, g) mixed layer depth ($\sigma_t = 0.03\,\mathrm{kg\,m^{-3}}$), and h) buoyancy flux. Overlain are the 500 m and 1000 m isobaths in m (brown and grey contours) and the 15 % sea ice concentration (green in a) and c), magenta in all other). The fjord names in Ammassalik are indicated in d) with KG: Køge Bugt Fjord, IK: Ikertivaq, and SF: Sermilik Fjord. The orange box in h) marks the Ammassalik area for which the water mass transformation has been calculated.

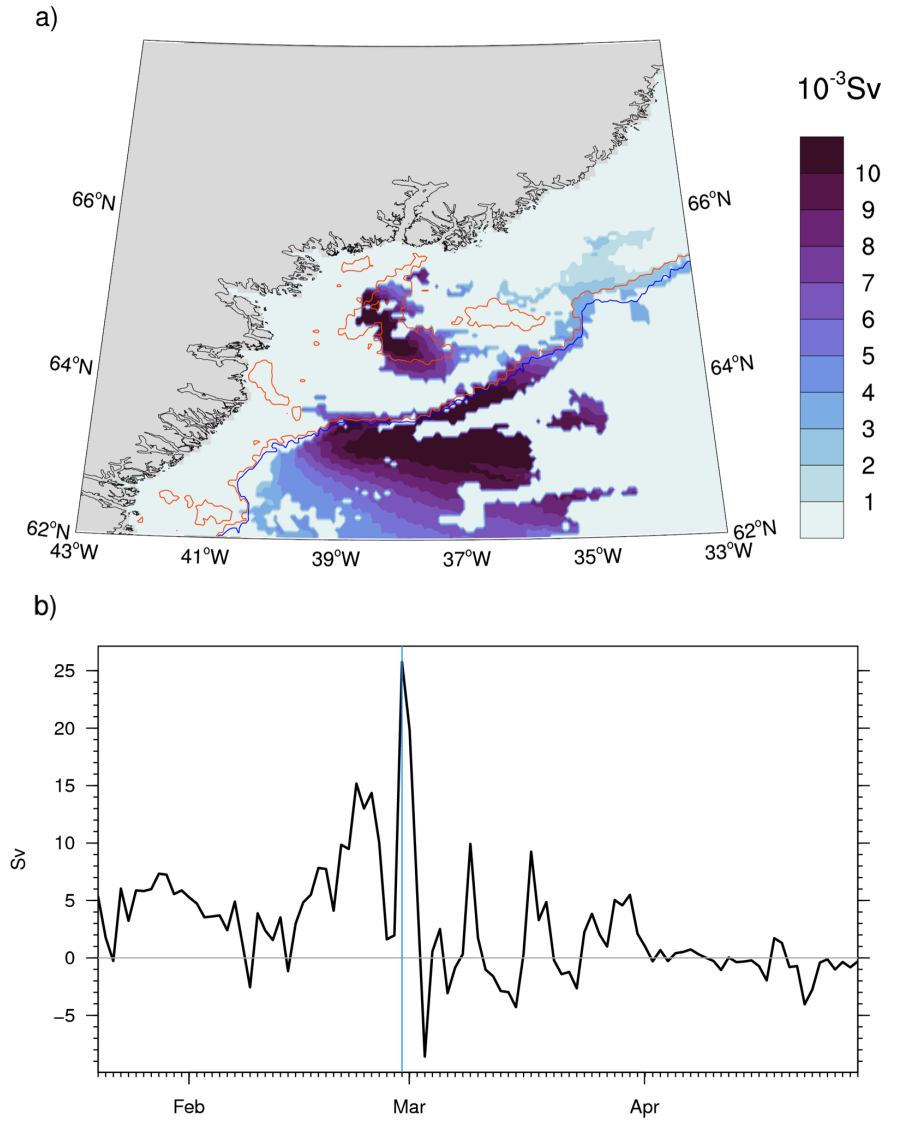


**Figure 4.** Water mass transformation (Sv) of density class $\sigma = 27.6 \pm 0.025\,\mathrm{kg\,m^{-3}}$ on a) 29 February 2020 during the katabatic storm. The coloured contours show the 500 m (orange) and 1000 m (blue) isobaths. b) time series of water mass transformation of same density class integrated over the area shown in a). The 29 February is marked by the vertical blue line.

The katabatic storm (daily means on 29 February 2020; Fig 3a) consists of two cones of high wind speeds that merge over the southeast Greenland shelf, one from Ikertivaq valley and the other from the Køge Bugt Fjord. We focus on the flow from the Ikertivaq valley because it directly passes over the Sermilik Trough (ST), a bathymetric feature that reaches depths of about 800 m (An et al., 2019). The ST has recently received attention because drifter data revealed that the East Greenland Current (EGC) steers northwards on its northern flank, where it interacts with the East Greenland Coastal Current (EGCC, Duyck & de Jong, 2021). Indeed, we find similar pathways of the EGC or EGIC in our simulation (Fig. 3b) that agree well with trajectories of these drifters. The main part of the EGIC flows along the shelf break, but a smaller fraction steers northward into the ST with even a pathway that directly crosses the trough, as described by Duyck and de Jong (2021).

The inflow of the relatively warm EGIC along the northern flank of the ST results in warmer sea surface temperatures of about 3 to 4.5 °C (Fig. 3c). These warmer SSTs in the northern ST could be the reason why there is no sea ice present in the Ammassalik area. After mixing with the colder and fresher EGCC, but also because of substantial heat loss to the atmosphere (Fig. 3e-f), the SSTs are colder (1.5 to 3 °C) in the return flow in the southern ST. The sensible and latent heat fluxes reach daily mean values of 1000 $\mathrm{W\,m^{-2}}$ over the ST during the event because of strong wind speeds and large temperature and moisture contrasts. The high wind speeds exert strong wind stress (Fig. 3d) on the upper ocean with positive wind stress curl over the ST that further contributes to convection in the ST.

At the shelf break, the cold katabatic flow encounters the warmer waters of the recirculating Irminger Current and the turbulent heat fluxes peak for a second time with values of about 700 $\mathrm{W\,m^{-2}}$ for the sensible heat flux and 600 $\mathrm{W\,m^{-2}}$ for the latent heat flux. The sensible heat flux is higher during the event because the air-sea contrast is stronger for temperature than for moisture.

The considerable heat loss from the ocean and momentum gain due to high wind stress leads to convection and vertical mixing in the ST and on the shelf break, which is visible as deep mixed layers ($\sigma_t = 0.03\,\mathrm{kg\,m^3}$; Fig. 3h) in the ST and as a narrow band along the shelf break. To quantify the effect of the katabatic storm on the ocean, we calculated the buoyancy flux (B) following Groeskamp et al. (2019), with a negative B meaning buoyancy loss of the ocean:

$$B = \overline{w'b'} = \frac{g\alpha}{\rho_0 c_p} Q_0 + g\beta S(P - E), \tag{2}$$

with $g$ the gravitational acceleration, $\rho_0 = 1025.022\,\mathrm{kg\,m^{-3}}$ the reference density, $Q_0$ the net heat flux (in $\mathrm{W\,m^{-2}}$) at the ocean surface (positive into the ocean), $\alpha$ and $\beta$ the thermal expansion and haline contraction coefficients, $S$ the salinity, $P$ the precipitation (in $\mathrm{m\,s^{-1}}$) and $E$ the evaporation (in $\mathrm{m\,s^{-1}}$). Note that we neglect the penetration of shortwave radiation into the ocean, as it is anyway very small in winter. The net heat flux at the ocean surface was calculated as:

$$Q_0 = Q_S + Q_L + Q_{SW} + Q_{LW}, \tag{3}$$

with $Q_S$ the sensible heat flux, $Q_L$ the latent heat flux, $Q_{SW}$ the net shortwave radiation and $Q_{LW}$ the net longwave radiation.

The buoyancy loss is mainly determined by the turbulent heat fluxes. It peaks over the ST and EGIC where the turbulent heat fluxes are largest, but there is also buoyancy loss in the central Irminger Basin (Fig. 3g). Although there is no deep convection during the simulated winter, these results suggest that katabatic storms can contribute to

precondition the Irminger Sea for deep convection. In contrast, a tip jet at Cape Farewell occurring at the same day induces a buoyancy loss only near the coast. Even though we analyze only a single event, the role of katabatic storms for triggering deep convection could be underestimated simply because the atmospheric resolution has so far been too coarse to resolve them. If true, katabatic winds could be of greater importance than has been attributed to them so far Paquin et al. (2016).

We estimate the water mass transformation $F(\sigma)$ ($\mathrm{m^3\,s^{-1}}$) for density classes (or bin size) enclosed by outcropping isopycnals of $\Delta\sigma = 0.05\,\mathrm{kg\,m^{-3}}$, following the approach of Petit et al. (2020) and Speer and Tziperman (1992). We calculate $F(\sigma)$ from daily mean values of the buoyancy flux:

$$F(\sigma) = \frac{1}{(g/\rho_0)\Delta\sigma} \iint -B\,\Pi\,(\sigma)\,dA, \tag{4}$$

where

$$\Pi(\sigma) = \begin{cases} 1, & \text{for } |\sigma - \sigma'| \leq \frac{\Delta\sigma}{2} \\ 0, & \text{otherwise} \end{cases} \tag{5}$$

with $A$ the area enclosed by a density class. $F(\sigma) > 0$ means that water is transformed to this density class. We chose $\Delta\sigma = 0.05\,\mathrm{kg\,m^{-3}}$ and show the result for the densest outcropping class of $\sigma = 27.6 \pm \Delta\sigma/2\,\mathrm{kg\,m^{-3}}$ during the katabatic storm on 29 February 2020 in Fig. 4a. Water mass transformation is largest in the ST and along the EGIC, with an area downstream that also includes part of the inner basin (Fig. 4a). Integrating over the area shown and considering the period from 20 January to 30 April 2020 shows that water mass transformation peaks during the katabatic storm. A day later, on 1 March, the Ammassalik area is still influenced by the storm and water transformation remains high before dropping sharply after the storm subsides.

## 5 Vertical transects along the Ikertivaq valley and Sermilik Trough

Transects of daily mean quantities for 29 February 2020 along the Ikertivaq valley and through the ST (Fig. 5) illustrate the air-sea interactions in the ST in more detail.

On 29 February 2020 the superimposed strong pressure gradients associated with the polar low cause velocities that reach almost $50\,\mathrm{m\,s^{-1}}$ over the steep slopes near the coast and result in a tongue of high wind speeds reaching up to $30\,\mathrm{m\,s^{-1}}$ in the lower 1000 m over the shelf (Fig.5a). Where the slopes are steepest, there is a hydraulic jump and the wind speed drops to very small values. This jump is associated with the breaking of a mountain wave as described in Oltmanns et al. (2015). The mountain wave breaking transfers momentum downwards, which can be seen by strong downward velocities (Fig. 5c) that accelerate the katabatic flow (see details how this affects the dynamics of the katabatic flow in Oltmanns et al. (2015)).

Over the ocean, the cold and dry air mass from the Greenland ice sheet (Fig. 5e) encounter the relatively warm water of the ST (Fig. 5d). Convection with cloud formation is initiated in the atmosphere due to the unstable stratification (Fig.5c). The clouds, however, move quickly with the flow so that only a small fraction is visible in the daily mean. The katabatic boundary layer is well visible from the potential temperature distribution (Fig. 5e) and is about 200 to 400 m thick, which is typical for southeast Greenland (Klein & Heinemann, 2002; Heinemann, 2003). As the cold and dry air mass warms and moistens over the shelf, the stable boundary layer evolves into a convective boundary layer, whose height increases with distance from the coast. The cold air outburst and the subsequent convection and cloud formation could also further intensify the polar low.

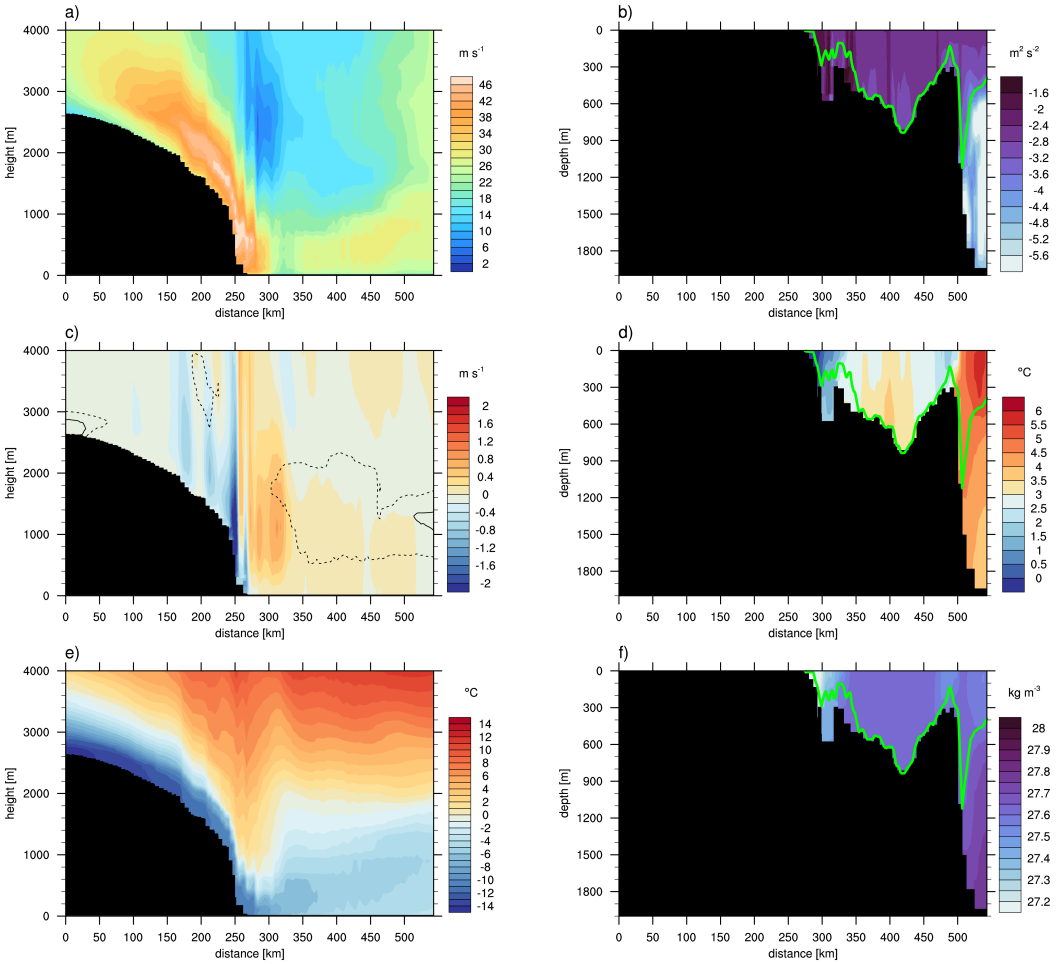


**Figure 5.** Vertical transects (daily means) along the Ikertivaq valley and Sermilik Trough: a) wind speed, b) turbulent kinetic energy in ocean, c) atmospheric vertical velocity with cloud cover (10 % dashed and 50 % solid contours), d) ocean potential temperature, e) atmospheric potential temperature, and f) ocean density ($\sigma_\Theta = \sigma - 1000\,\mathrm{kg\,m^{-3}}$). The green line in b), d), and f) marks the depth of the mixed layer ($\sigma_\Theta = 0.03\,\mathrm{kg\,m^{-3}}$).

The strong wind stress and heat fluxes cause intense vertical mixing and buoyancy loss in the ST, resulting in large values of TKE (Fig.5b) reaching $10^{-2}\,\mathrm{m^2\,s^{-1}}$ near the surface. In fact, the entire water column in the ST is mixed, as can be seen from the mixed layer reaching the bottom and the homogeneous density (Fig.5f) with the $27.6\,\mathrm{kg\,m^{-3}}$ isopycnal outcropping at the surface. However, the water mass is not homogeneous as there is still structure in the temperature and salinity fields. The heat loss and the subsequent cooling results in a mixed layer with densities of about $\sigma_\theta = 27.6$ to $27.65\,\mathrm{kg\,m^{-3}}$. This density on the shelf and shelf break is close to the recently identified uISIW ($\sigma_\theta = 27.65$ to $27.73\,\mathrm{kg\,m^{-3}}$) that forms at the edge of the western boundary (LeBras et al., 2020).

The relatively warm temperatures of the EGIC induce a secondary peak of turbulent heat flux and negative buoyancy flux at the shelf break, leading to densities in the boundary current similar to those in the ST and a mixed layer depth of about 1100 m. Dense water then leaves the ST and flows into the lower boundary current over the course of the next couple of days (not shown). Both processes cause a densification of the boundary current and thus contribute to the sinking of Atlantic water in the Irminger Sea. The density anomalies are then transported downstream where they can even reach the Labrador Sea.

## 6 Summary and conclusions

We have analyzed a mesoscale katabatic storm event of hurricane intensity over the Irminger Sea and how it interacts with the ocean in the fully coupled, global climate model ICON-ESM with storm-resolving (5 km) resolution. Katabatic storms have not been resolved hitherto in global models because of its small spatial extent, in particular in the narrow valleys and fjords of Greenland. Our study is the first in which such an event and its interactions with the ocean and feedback with the large-scale synoptics is simulated in a global coupled climate model.

ICON-ESM is able to represent katabatic storms and other mesoscale wind systems around Greenland with details previously described only by regional climate models. It captures the complex interaction of the circulation with the steep orography of southeast Greenland. A polar low forms within a lee trough environment over the Irminger Sea that is initially triggered by the katabatic flow from the Ammassalik valleys. The superimposed pressure gradient of the polar low accelerates the katabatic flow into a storm but also deepens the upper-level trough. These results demonstrate the importance of resolving the feedback of the small scales to the large scale in global climate models and emphasizes the synoptic relevance of the Irminger Sea.

High resolution in the ocean allows resolving small-scale bathymetric features of the southeast Greenland shelf, such as the Sermilik Trough, where the EGC interacts with the EGCC and where water mass transformation takes place. Strong air-sea fluxes caused by the katabatic storm induce substantial heat loss from the ocean and transfer momentum to it. As a result, convection and mixing is induced in the Sermilik Trough and along the shelf break, leading to density anomalies in the trough and boundary current. Previous studies have shown that density anomalies in the boundary current of the Irminger Sea caused by surface fluxes strongly influence AMOC variability.

The water mass formed within the Sermilik Trough and on the shelf during the katabatic storm has a density that is close to the recently described upper Irminger Sea Intermediate Water. Even though our simulation is rather short, we conclude that katabatic storms are relevant for the densification of the western boundary current. Experiments covering several decades with this class of models will be carried out in the European Union "NextGEMs" project (`https://nextgems-h2020.eu`). These simulations provide opportunities to explore further how dense water masses formed in the ST and

at the shelf edge together with denser water masses from deep convection and the overflows contribute to North Atlantic Deep water and its variability.

## Open Research

Primary scripts to reproduce the figures and analyses can be obtained from MPG.PuRe (`http://hdl.handle.net/21.11116/0000-0008-ECF1-E`, Gutjahr, Jungclaus, Brüggemann, et al., 2021) and the model data from the WDCC Long Term Archive (`http://cera-www.dkrz.de/WDCC/ui/Compact.jsp?acronym=DKRZ_LTA_033_ds00010`, Gutjahr, Jungclaus, Brüggemann, et al., 2021). The model code of ICON is available to individuals under licenses (`https://mpimet.mpg.de/en/science/modeling-with-icon/code-availability`). The buoyancy fluxes and the water mass transformation were calculated with R 4.0.2 (R Core Team, 2020) and the oce package version 1.3-0 (Kelley & Richards, 2021).

## Acknowledgments

This work is a contribution to the project S2 (Improved Parameterizations and Numerics in Climate Models) of the Collaborative Research Centre TRR 181 "Energy Transfer in Atmosphere and Ocean" funded by the Deutsche Forschungsgemeinschaft (DFG, German Research Foundation) - project number 274762653 and the Max Planck Society for the Advancement of Science. The research was supported by the European Union Horizon 2020 collaborative project NextGEMS (grant number 101003470). DYAMOND data management was provided by the Deutsches Klimarechenzentrum (DKRZ) and supported through the projects ESiWACE and ESiWACE2. The projects ESiWACE and ESiWACE2 have received funding from the European Union's Horizon 2020 research and innovation program under grant agreements No 675191 and 823988. This work used resources of the Deutsches Klimarechenzentrum (DKRZ) granted by its Scientific Steering Committee (WLA) under project IDs bk1040 and bb1153. We thank the DYAMOND Winter (`https://www.esiwace.eu/services/dyamond/winter`) team at MPI-M and DKRZ for producing the simulation. We further thank Elisa Manzini for providing constructive comments.

## References

An, L., Rignot, E., Chauche, N., Holland, D., Holland, D., Jakobsson, M., ... Willis, J. K. (2019). Bathymetry of southeast Greenland from oceans melting Greenland (OMG) data. *Geophysical Research Letters*, *46*, 11197–11205. doi: 10.1029/2019GL083953

Bacon, S., Gould, W. J., & Jia, Y. L. (2003). Open-ocean convection in the Irminger Sea. *Geophys. Res. Lett.*, *30*, 1246. doi: 10.1029/2002GL016271

Blanke, B., & Delecluse, P. (1993). Variability of the Tropical Atlantic Ocean Simulated by a General Circulation Model with Two Different Mixed-Layer Physics. *J. Phys. Oceanogr.*, *23*(7), 1363–1388. doi: 10.1175/1520-0485(1993)023⟨1363:VOTTAO⟩2.0.CO;2

Blechschmidt, A.-M., Bakan, S., & Graßl, H. (2009). Large-scale atmospheric circulation patterns during polar low events over the Nordic seas. *J. Geophys. Res.*(D06115). doi: 10.1029/2008JD010865

Bracegirdle, T. J., & Gray, S. L. (2008). An objective climatology of the dynamical forcing of polar lows in the Nordic Seas. *Int. J. Climatol.*, *28*, 1903–1919. doi: 10.1002/joc.1686

Bracegirdle, T. J., & Gray, S. L. (2009). The dynamics of a polar low assessed using potential vorticity inversion. *Quarterly Journal of the Royal Meteorological Society*, *135*, 880–893. doi: 10.1002/qj.411

Chafik, L., & Rossby, T. (2019). Volume, Heat, and Freshwater Divergences in the Subpolar North Atlantic Suggest the Nordic Seas as Key to the State of

519 the Meridional Overturning Circulation. *Geophysical Research Letters*, *46*,
520 4799–4808. doi: 10.1029/2019GL082110
521 Condron, A., Bigg, G. R., & Renfrew, I. A. (2008). Modeling the impact of polar
522 mesocyclones on ocean circulation. *J. Geophys. Res.*, *113*(C10005). doi: 10
523 .1029/2007JC004599
524 de Jong, M. F., Oltmanns, M., Karstensen, J., & de Steur, L. (2018). Deep Convec-
525 tion in the Irminger Sea Observed with a Dense Mooring Array. *Oceanography*,
526 *31*, 50–59. doi: 10.5670/oceanog.2018.109
527 de Jong, M. F., van Aken, H. M., Våge, K., & Pickart, R. S. (2012). Convective mix-
528 ing in the central Irminger Sea: 2002–2010. *Deep-Sea Res. I*, *63*, 36–51. doi:
529 10.1016/j.dsr.2012.01.003
530 Desbruyères, D., Mercier, H., Maze, G., & Daniault, N. (2019). Surface predic-
531 tor of overturning circulation and heat content change in the subpolar North
532 Atlantic. *Ocean Sci.*. doi: 10.5194/os-15-809-2019
533 Dierer, S., & Schluenzen, K. H. (2005). Influence parameters for a polar mesocy-
534 clone development. *Meteorologische Zeitschrift*, *14*, 781-792. doi: 10.1127/0941
535 -2948/2005/0077
536 Dipankar, A., Stevens, B., Heinze, R., Moseley, C., Zängl, G., Giorgetta, M., & Br-
537 dar, S. (2015). Large eddy simulation using the general circulation model
538 ICON. *J. Adv. Model. Earth Syst.*, *7*, 963–986. doi: 10.1002/2015MS000431
539 DuVivier, A. K., & Cassano, J. J. (2013). Evaluation of WRF Model Resolution on
540 Simulated Mesoscale Winds and Surface Fluxes near Greenland. *Mon. Weather*
541 *Rev.*, *141*(3), 941–963. doi: 10.1175/MWR-D-12-00091.1
542 Duyck, E., & de Jong, M. F. (2021). Circulation over the South-East Greenland
543 Shelf and Potential Freshwater Export: a Drifter Study. *Geophysical Research*
544 *Letters*, *48*, e2020GL091948. doi: 10.1029/2020GL091948
545 Eady, E. (1949). Long waves and cyclone waves. *Tellus*, *1*, 33–52. doi: 10.1111/
546 j.2153-3490.1949.tb01265.x
547 Eyring, V., Bony, S., Meehl, G. A., Senior, C. A., Stevens, B., Stouffer, R. J., &
548 Taylor, K. E. (2016). Overview of the Coupled Model Intercomparison Project
549 Phase 6 (CMIP6) experimental design and organization. *Geosci. Model Dev.*,
550 *9*, 1937–1958. doi: 10.5194/gmd-9-1937-2016
551 Gaspar, P., Grégoris, Y., & Lefevre, J.-M. (1990). A simple eddy kinetic energy
552 model for simulations of the oceanic vertical mixing: Tests at station Papa
553 and long-term upper ocean study site. *J. Geophys. Res. Oceans*, *95*(C9),
554 16179–16193. doi: 10.1029/JC095iC09p16179
555 Giorgetta, M. A., Brokopf, R., Crueger, T., Esch, M., Fiedler, S., Helmert, J., ...
556 Stevens, B. (2018). ICON-A, the Atmosphere Component of the ICON Earth
557 System Model: I. Model Description. *Journal of Advances in Modeling Earth*
558 *Systems*, *10*, 1613–1637. doi: 10.1029/2017MS001242
559 Giorgi, F. (2019). Thirty years of regional climate modelling: where are we and
560 where are we going next? *Journal of Geophysical Research: Atmospheres*, *124*,
561 5696–5723. doi: 10.1029/2018JD030094
562 Groeskamp, S., Griffies, S. M., Iudicone, D., Marsh, R., Nurser, A. J. G., & Zika,
563 J. D. (2019). The Water Mass Transformation Framework for Ocean Physics
564 and Biogeochemistry. *Annual Review of Marine Science*, *11*, 271–305. doi:
565 10.1146/annurev-marine-010318-095421
566 Gutjahr, O., & Heinemann, G. (2018). A model-based comparison of extreme winds
567 in the Arctic and around Greenland. *Int. J. Climatol.*, *38*, 5272–5292. doi: 10
568 .1002/joc.5729
569 Gutjahr, O., Jungclaus, J. H., Brüggemann, N., Haak, H., & Marotzke, J. (2021).
570 *Air-sea interactions and water mass transformation during a katabatic storm*
571 *in the Irminger Sea – Scripts.* Retrieved from `http://hdl.handle.net/`
572 `21.11116/0000-0008-ECF1-E` (last access: 07.10.2021)
573 Gutjahr, O., Jungclaus, J. H., Brüggemann, N., Haak, H., & Marotzke, J. (2021).

*Air-sea interactions during a katabatic storm in the Irminger Sea simulated by a globally coupled storm-resolving (5 km) climate model - ICON Dyamond Winter simulation data.* World Data Center for Climate (WDCC) at DKRZ. Retrieved from `http://cera-www.dkrz.de/WDCC/ui/Compact.jsp?acronym=DKRZ\_LTA\_033\_ds00010` (last access: 03.08.2021)

Haarsma, R. J., Roberts, M. J., Vidale, P. L., Senior, C. A., Bellucci, A., Bao, Q., ... von Storch, J.-S. (2016). High Resolution Model Intercomparison Project (HighResMIP v1.0) for CMIP6. *Geosci. Model Dev.*, *9*(11), 4185–4208. doi: 10.5194/gmd-9-4185-2016

Heinemann, G. (2003). Forcing and feedback mechanisms between the katabatic wind and sea ice in the coastal areas of polar ice sheets. *The Global Atmosphere and Ocean System*, *9*(4), 169–201. doi: 10.1080/1023673042000198130

Heinemann, G., & Klein, T. (2002). Modelling and observations of the katabatic flow dynamics over Greenland. *Tellus A: Dynamic Meteorology and Oceanography*, *54*(5), 542–554. doi: 10.3202/tellusa.v54i5.12167

Hersbach, H., Bell, B., Berrisford, P., Hirahara, S., Horányi, A., Muñoz-Sabater, J., ... Thépaut, J.-N. (2020). The ERA5 global reanalysis. *Quarterly Journal of the Royal Meteorological Society*, *146*(730), 1999–2049. doi: https://doi.org/10.1002/qj.3803

Hoskins, B. J., McIntyre, M. E., & Robertson, A. W. (1985). On the use and significance of isentropic potential vorticity maps. *Q. J. R. Meteorol.*, *111*, 877–946. doi: 10.1002/qj.49711147002

Jungclaus, J., Lorenz, S. J., Schmidt, H., Brovkin, V., Brüggemann, N., Chegini, F., ... Claussen, M. (2021). The ICON Earth System Model Version 1.0. *Earth and Space Science Open Archive*, 44. doi: 10.1002/essoar.10507989.1

Kalnay, E., Kanamitsu, M., Kistler, R., Collins, W., Deaven, D., Gandin, L., ... Joseph, D. (1996). The ncep/ncar 40-year reanalysis project. *Bulletin of the American Meteorological Society*, *77*(3), 437 - 472. Retrieved from `https://journals.ametsoc.org/view/journals/bams/77/3/1520-0477_1996_077_0437_tnyrp_2_0_co_2.xml` doi: 10.1175/1520-0477(1996)077⟨0437:TNYRP⟩2.0.CO;2

Kelley, D., & Richards, C. (2021). oce: Analysis of oceanographic data [Computer software manual]. Retrieved from `https://CRAN.R-project.org/package=oce` (R package version 1.3-0)

Klaver, R., Haarsma, R., Vidale, P. L., & Hazeleger, W. (2020). Effective resolution in high resolution global atmospheric models for climate studies. *Atmos Sci Lett.*, *21*, e952. doi: 10.1002/asl.952

Klein, T., & Heinemann, G. (2002). Interaction of katabatic winds and mesocyclones near the eastern coast of Greenland. *Meteorol. Appl.*, *9*, 407–422. doi: 10.1017/S1350482702004036

Kolstad, E. W. (2011). A global climatology of favourable conditions for polar lows. *Quarterly Journal of the Meteorological Society*, *137*, 1749–1761. doi: 10.1002/qj.888

Kolstad, E. W., Bracegirdle, T. J., & Seierstad, I. A. (2009). Marine cold-air outbreaks in the North Atlantic: temporal distribution and associations with large-scale atmospheric circulation. *Clim. Dynam.*, *33*, 187–197. doi: 10.1007/s00382-008-0431-5

Korn, P. (2017). Formulation of an unstructured grid model for global ocean dynamics. *J. Comp. Physiol.*, *339*, 525–552. doi: 10.1016/j.jcp.2017.03.009

Kristjánsson, J. E., Thorsteinsson, S., Kolstad, E. W., & Blechschmidt, A.-M. (2011). Orographic influence of east Greenland on a polar low over the Denmark Strait. *Quarterly Journal of the Meteorological Society*, *137*, 1773–1789. doi: 10.1002/qj.831

LaCasce, J. H., & Groeskamp, S. (2020). Baroclinic Modes over Rough Bathymetry and the Surface Deformation Radius. *J. Phys. Oceanogr.*, *50*, 2835–2847. doi:

10.1175/JPO-D-20-0055.1

Landgren, O. A., Batrak, Y., Haugen, J. E., Støylen, E., & Iversen, T. (2019). Polar low variability and future projections for the Nordic and Barents Seas. *Quarterly Journal of the Royal Meteorological Society*, *145*(724), 3116-3128. Retrieved from `https://rmets.onlinelibrary.wiley.com/doi/abs/10.1002/qj.3608` doi: https://doi.org/10.1002/qj.3608

LeBras, I. A.-A., Straneo, F., Holte, J., de Jong, M. F., & Holliday, N. P. (2020). Rapid export of waters formed by convection near the Irminger Sea's western boundary. *Geophysical Research Letters*, *47*(e2019GL085989). doi: 10.1029/2019GL059898

Leduc, M., & Laprise, R. (2009). Regional climate model sensitivity to domain size. *Climate Dynamics*, *32*, 833–854. doi: 10.1007/s00382-008-0400-z

Lindzen, R., & Farrell, B. (1980). A simple approximate result for the maximum growth rate of baroclinic instabilities. *Journal of the Atmospheric Sciences*, *37*, 1648–1654.

Lozier, M. S., Li, F., Bacon, S., Bahr, F., Bower, A. S., Cunningham, S. A., ... Zhao, J. (2019). A sea change in our view of overturning in the subpolar North Atlantic. *Science*, *363*(6426), 516–521. doi: 10.1126/science.aau6592

Mc Innes, H., Kristiansen, J., Kristjánsson, J. E., & Schyberg, H. (2011). The role of horizontal resolution for polar low simulations. *Q. J. R. Meteorol. Soc.*, *137*(660), 1674–1687. doi: 10.1002/qj.849

Mc Innes, H., Kristjánsson, J. E., Schyberg, H., & Røsting, B. (2009). An assessment of a Greenland lee cyclone during the Greenland Flow Distortion experiment: An observational approach. *Quarterly Journal of the Meteorological Society*, *135*, 1968–1985. doi: 10.1102/qj.524

Menary, M. B., Jackson, L., & Lozier, M. S. (2020). Reconciling the Relationship Between the AMOC and Labrador Sea in OSNAP Observations and Climate Models. *Geophysical Research Letters*, *47*, e2020GL089793. doi: 10.1029/2020GL089793

Moreno-Ibáñez, M., Laprise, R., & Gachon, P. (2021). Recent advances in polar low research: current knowledge, challenges and future perspectives. *Tellus A: Dynamic Meteorology and Oceanography*, *73*(1), 1–31. doi: 10.1080/16000870.2021.1890412

Neumann, P., Düben, P., Adamidis, P., Bauer, P., Brück, M., Kornblueh, L., ... Biercamp, J. (2019). Assessing the scales in numerical weather and climate predictions: will exascale be the rescue? *Phil. Trans. R. Soc. A*, *377*, 20180148. doi: 10.1098/rsta.2018.0148

Oltmanns, M., Straneo, F., Moore, G. W. K., & Mernild, S. H. (2014). Strong downslope wind events in Ammassalik, southeast Greenland. *J. Climate*, *27*, 977–993. doi: 10.1175/jcli-d-13-00067.1

Oltmanns, M., Straneo, F., Seo, H., & Moore, G. W. K. (2015). Role of Wave Dynamics and Small-Scale Topography for Downslope Wind Events in Southeast Greenland. *Journal of the Atmospheric Sciences*, *72*, 2786–2805. doi: 10.1175/JAS-D-14-0257.1

Paquin, J.-P., Lu, Y., Higginson, S., Dupont, F., & Garric, G. (2016). Modelled variability of deep convection in the Irminger Sea during 2003–10. *J. Phys. Oceanogr.*, *46*, 179–196. doi: 10.1175/JPO-D-15-0078.1

Petit, T., Lozier, M. S., Josey, S. A., & Cunningham, S. A. (2020). Atlantic Deep Water Formation Occurs Primarily in the Iceland Basin and Irminger Sea by Local Buoycancy Forcing. *Geophys. Res. Lett.*, *47*, e2020GL091028. doi: 10.1029/2020GL091028

Pickart, R. S., Spall, M. A., Ribergaard, M. H., Moore, G. W. K., & Milliff, R. F. (2003). Deep convection in the Irminger Sea forced by the Greenland tip jet. *Nature*, *424*(6945), 152–156. doi: 10.1038/nature01729

R Core Team. (2020). R: A language and environment for statistical computing

[Computer software manual]. Vienna, Austria. Retrieved from `https://www.R-project.org/`

Rasmussen, L. (1989). Greenland winds and satellite imagery. *Vejret-Danish Meteor. Soc.*, 32–37.

Rühs, S., Oliver, E. C. J., Biastoch, A., Böning, C. W., Dowd, M., Getzlaff, K., ... Myers, P. G. (2021). Changing Spatial Patterns of Deep Convection in the Subpolar North Atlantic. *Journal of Geophysical Research: Oceans*, *126*(7), e2021JC017245. doi: https://doi.org/10.1029/2021JC017245

Simmons, A., & Gibson, J. (2000, 03). The era-40 project plan. (1), 62. Retrieved from `https://www.ecmwf.int/node/12272`

Skamarock, W. C. (2004). Evaluating Mesoscale NWP Models Using Kinetic Energy Spectra. *Mon. Weather Rev.*, *132*(12), 3019–3032. doi: 10.1175/MWR2830.1

Speer, K., & Tziperman, E. (1992). Rates of water mass formation in the North Atlantic ocean. *J. Phys. Oceanogr.*, *22*, 93–104. doi: 10.1175/1520-0485(1992)022⟨0093:ROWMFI⟩2.0.CO;2

Steele, M., Morley, R., & Ermold, W. (2001). PHC: A global ocean hydrography with a high quality Arctic Ocean. *J. Climate*, *14*, 2079–2087.

Stevens, B., Satoh, M., Auger, L., Biercamp, J., Bretherton, C., Chen, X., ... Zhou, L. (2019). DYAMOND: The DYnamics of the Atmospheric circulation Modeled On Non-hydrostatic Domains. *Progress in Earth and Planetary Science*, *6*(61). doi: 10.1186/s40645-019-0304-z

Stoll, P. J., Graversen, R. G., Noer, G., & Hodges, K. (2018). An objective global climatology of polar lows based on reanalysis data. *Quarterly Journal of the Royal Meteorological Society*, *144*(716), 2099–2117. doi: https://doi.org/10.1002/qj.3309

Xia, L., Zahn, M., Hodges, K. I., Feser, F., & von Storch, H. (2012). A comparison of two identification and tracking methods for polar lows. *Tellus A: Dynamic Meteorology and Oceanography*, *64*(1), 17196. doi: 10.3402/tellusa.v64i0.17196

Yeager, S., Castruccio, F., Chang, P., Danabasoglu, G., Maroon, E., Small, J., ... Zhang, S. (2021). An outsized role for the Labrador Sea in the multidecadal variability of the Atlantic overturning circulation. *Science Advances*, *7*(41), eabh3592. doi: 10.1126/sciadv.abh3592

Zahn, M., & von Storch, H. (2008). A long-term climatology of North Atlantic polar lows. *Geophys. Res. Lett.*, *35*, L22702. doi: 10.1029/2008GL035769

Zängl, G., Reinert, D., Rípodas, P., & Baldauf, M. (2015). The ICON (ICOsahedral Non-hydrostatic) modelling framework of DWD and MPI-M: Description of the non-hydrostatic dynamical core. *Quarterly Journal of the Royal Meteorological Society*, *141*, 563–579. doi: 10.1002/qj.2378